Review Article

Satoshi Hasegawa* and Yoshio Hayasaki

Holographic femtosecond laser manipulation for advanced material processing

DOI 10.1515/aot-2015-0062
Received December 18, 2015; accepted February 1, 2016; previously published online February 25, 2016

Abstract: Parallel femtosecond laser processing using a computer-generated hologram displayed on a spatial light modulator, known as holographic femtosecond laser processing, provides the advantages of high throughput and high-energy use efficiency. Therefore, it has been widely used in many applications, including laser material processing, two-photon polymerization, two-photon microscopy, and optical manipulation of biological cells. In this paper, we review the development of holographic femtosecond laser processing over the past few years from the perspective of wavefront and polarization modulation. In particular, line-shaped and vector-wave femtosecond laser processing are addressed. These beam-shaping techniques are useful for performing large-area machining in laser cutting, peeling, and grooving of materials and for high-speed fabrication of the complex nanostructures that are applied to material-surface texturing to control tribological properties, wettability, reflectance, and retardance. Furthermore, issues related to the nonuniformity of diffraction light intensity in optical reconstruction and wavelength dispersion from a computer-generated hologram are addressed. As a result, large-scale holographic femtosecond laser processing over 1000 diffraction spots was successfully demonstrated on a glass sample.

Keywords: computer-generated hologram; cylindrical vector beam; femtosecond laser processing; laser beam shaping; spatial light modulator.

***Corresponding author: Satoshi Hasegawa,** Center for Optical Research and Education (CORE), Utsunomiya University, 7-1-2 Yoto, Utsunomiya 321-8585, Japan, e-mail: hasegawa_s@opt.utsunomiya-u.ac.jp
Yoshio Hayasaki: Center for Optical Research and Education (CORE), Utsunomiya University, 7-1-2 Yoto, Utsunomiya 321-8585, Japan

www.degruyter.com/aot

1 Introduction

Femtosecond laser processing [1, 2] is a promising tool for fabricating three-dimensional (3D) optical devices in transparent materials. In order to fabricate such optical devices at the millimeter scale, an enormous number of processing points are required, and therefore, the processing throughput must be improved. To address this issue, parallel femtosecond laser processing based on an array of spots has been proposed. Several methods have been used to demonstrate parallel laser processing, including methods using multibeam interference [3–5], microlens arrays [6, 7], and diffractive optical elements (DOEs) [8, 9]. Computer-generated holograms (CGHs) enable arbitrary control of the spatial pulse shape, and spatial light modulators (SLMs) displaying a dynamic CGH have been used to achieve variable spatial shaping of femtosecond pulses [10–12]. Femtosecond laser processing with a CGH, known as holographic femtosecond laser processing [10–40], has the advantages of high-throughput pulsed irradiation and highly energy-efficient use of the pulse and has been used in many applications, such as two-photon polymerization [13–17], optical waveguide fabrication [18–21], fabrication of volume phase gratings in polymers [22], surface structuring of silicon [23], and cell transfection [24].

In the development of holographic femtosecond laser processing, 3D parallel fabrication with single shots using a Fresnel CGH has been demonstrated [12, 25, 26]. The fabrication of high-aspect ratio nanochannels into glass using single-shot femtosecond Bessel beams generated by an axicon lens has also been reported [27]. In 3D fabrication in transparent materials, the spherical aberrations induced by a potential refractive index mismatch between the immersion medium of the microscope objective and the fabrication substrate represent a critical issue. To address this issue, CGH design methods with aberration correction have been proposed and applied to parallel laser processing [28, 29]. On the other hand, line-shaped femtosecond beams using a holographic cylindrical lens have been applied to laser cutting, peeling, and grooving of materials for two-dimensional (2D) large-area

machining with high throughput [30]. In order to develop a high-speed laser processing system and fabricate aperiodic structures, a CGH has been used in combination with high-speed galvanometer scanners [31, 32] and a microlens array [33].

In holographic femtosecond laser processing, many factors influence the morphology of the processed structures, such as the spatial intensity distribution and the temporal shape of the pulse diffracted by the CGH, as well as the aberrations (spatial dispersion) and temporal dispersion of optical elements in the system. In particular, precise control of the diffraction peaks from the CGH is important in large-scale parallel laser processing with an enormous number of nanometer-scale structures because the size of the structures strongly depends on the pulse energy close to the threshold. Therefore, optimization methods for obtaining a high-quality CGH have been proposed [34–40]. In one report, a method of optimizing a CGH based on parallel second harmonic generation has been demonstrated [39]. The method, which is called second harmonic optimization, incorporates the width and spatial profile of the pulse, which depend on the pulse peak intensity, into the CGH design. Estimation of the pulse peak intensity is essential in precision laser processing because femtosecond laser processing is performed on the basis of nonlinear absorption. With this method, high-quality parallel laser processing has been demonstrated.

In addition, the spatial dispersion caused by wavelength dispersion of the CGH considerably affects the processing quality. Spatial wavelength dispersion causes focal spot distortion and spatiotemporal spreading of the pulse in holographic femtosecond laser processing. In particular, when using sub-100 fs pulses – that is, a light source with a large spectral bandwidth – wavelength dispersion should be controlled in order to generate a high-quality beam. The effect of spatial dispersion on the morphology of the processed structures has been investigated in the processing of a glass surface with a holographic femtosecond laser processing system using an objective lens with a high numerical aperture (NA) and an energy near the threshold energy under the large-dispersion condition [41]. Some spatial and temporal dispersion compensation methods with special optical arrangements for holographic femtosecond laser processing have also been reported [8, 42–46]. These methods, based on a pair of DOEs, are useful techniques. In one report, dynamic control of spatial wavelength dispersion in a laser processing system composed of a pair of SLMs displaying two types of CGH, one for diffracting an incoming pulse and the other for compensating for angular separation of the diffraction pulse, has been demonstrated [47]. The CGH designed to control the dispersion is flexibly changed according to an arbitrary CGH designed to diffract the incoming pulse by taking advantage of the rewritable capability of the SLMs. The dispersion control drastically improves focal spot distortion and effectively restrains undesired processing by the 0th-order pulse in CGH reconstruction.

Conventional holographic femtosecond laser processing employs the basic principle of wavefront modulation using a CGH. To improve femtosecond laser processing, full control of degrees of freedom in the light, including amplitude, phase, and polarization is important. Such control entails exploiting the nature of light as a vector wave. Manipulation of the polarization state of femtosecond laser pulses has also played a significant role in various applications because it provides efficient control of light-matter interactions. In particular, a light field with spatially inhomogeneous states of polarization, called a vector beam, has attracted attention due to its novel properties, such as selective excitation of anisotropic molecules [48], observation of the 3D orientation of single molecules [49], focusing to a spot size beyond the diffraction limit by virtue of the longitudinal vector component (z-polarization) of a radially polarized beam focused by a high-numerical-aperture objective lens [50], and fabrication of periodic nanostructures aligned perpendicularly to the polarization direction of the femtosecond laser light by virtue of the interaction between the light and a surface plasmon wave [51]. In the irradiation directed at a sample using a radially and azimuthally polarized beam, each polarization component at the focal point behaves as a pure p- or s-polarization [52]. The reflectance of light associated with s-polarization is usually larger than that associated with p-polarization at a large incident angle. In particular, reflectance differs drastically in the laser processing of metal materials. Therefore, a radially polarized beam is useful for effective laser cutting [53] because the beam interacts with the material while constantly maintaining p-polarization regardless of the beam sweep direction. An azimuthally polarized beam, on the other hand, is effective for laser drilling [54] because the wall of the hole is highly reflective to the s-polarized light and does not absorb the incident beam, allowing most of the power to reach the bottom of the hole. A report has also demonstrated that the trapping efficiency of optical tweezers [55] is improved because the reflectance of the particle to the incident light is decreased. Therefore, a femtosecond vector beam has the potential to expand the functionality of existing optical systems and to support the development of novel applications in various research fields.

We originally demonstrated holographic femtosecond laser processing with polarization distribution control

using a pair of SLMs [56]. In the report, the azimuthal angles of linear polarization in parallel beams composed of an array of spots were individually controlled. As a result, the interval between the diffraction spots was minimized by avoiding mutual interference; the interval was reduced by half compared with our previous work [40]. Fabrication of the complex 2D subwavelength microstructures induced by femtosecond vector light fields using an SLM and a grating has been presented [57]. In addition, holographic picosecond laser processing involving a dynamical change among four polarization states, including linear horizontal and vertical states, a radial state, and an azimuthal state, has also been demonstrated for a stainless steel sample [58]. Recently, laser processing with 2D [59, 60] and 3D [61] reconstruction including multiple radial and azimuthal beams, known as holographic vector-wave laser processing, has also been reported. These reconstructions with more complicated polarization fields are important for fabricating an orientation-controlled nanostructure. Material-surface nanostructuring is useful for controlling tribological properties [62], wettability [63], reflectance [64], and retardance [65].

In this paper, we review our results from the past few years regarding holographic femtosecond laser manipulation for advanced material processing. Key aspects of realizing a holographic manipulation using the femtosecond laser and its applications to laser processing are carefully discussed by analyzing these experimental results. In addition, our latest achievement related to holographic laser processing with polarization control is presented. In Section 2, femtosecond laser processing with a holographic line-shaped beam for large-area machining is described. In Section 3, large-scale holographic femtosecond laser processing achieved by a CGH design algorithm for high-quality reconstruction is demonstrated. In Section 4, dynamic control of spatial wavelength dispersion to improve focal spot quality in holographic femtosecond laser processing is presented. In Section 5, recent progress on holographic vector-wave femtosecond laser processing is summarized. In Section 6, we conclude our paper.

2 Femtosecond laser processing with a holographic line-shaped beam

2.1 Principle of generation of a line-shaped beam

For a wide-area fabrication in realistic applications, a linear beam offers a considerably higher processing throughput than an ordinary Gaussian beam because the total length of the beam scanning area is reduced and the mechanical constraints on the throughput are relaxed. In addition to these quantitative advantages, line-beam processing has qualitative advantages. One is the absence of artifacts derived from the scanning of a focused beam. Owing to an overlapping of the focused beam, conventional beam scanning may produce a derivative structure aligned perpendicularly to the scanning direction depending on the beam parameters, including spot size and pulse repetition rate. In line-beam processing, there is no derivative structure in the beam irradiation area because the light intensity is smoothly continuous. The other advantage is less debris; because the direction of the flying debris is parallel to the scanning direction of the beam, part of the debris is removed by the laser beam itself [66]. Therefore, line-shaped femtosecond pulses are well suited to large-area machining with high throughput in laser cutting, peeling, and grooving of materials.

The phase distribution of a holographic cylindrical lens designed to generate a line-shaped beam is described by

$$u(x, y)=w(x)\left(\frac{ky^2}{2f}\right) \bmod (2\pi), \tag{1}$$

where $w(x)$ is a window function with a value from 0 to 1, $k=2\pi/\lambda$ is the wave number, and f is the focal length. In this experiment, f was set to 2000 mm. Figure 1 shows the two types of holographic cylindrical lenses that we used, their different $w(x)$ functions, and their computational reconstructions at different propagation distances from the SLM. When $w(x)$ was a rectangular function given by

$$w_{\mathrm{rect}}(x)=\begin{cases}1 \text{ if } 0\le x<1\\ 0 \quad \text{else}\end{cases}, \tag{2}$$

the diffraction image was a long line-shaped beam, but oscillations due to diffraction caused by the edges of the aperture were present, as shown in Figure 1A. A smoothly decaying window function suppresses diffraction from the edges. We used a modified form of the Akaike window, described by

$$w_{\mathrm{mak}}(x)=\begin{cases}w_{\mathrm{akaike}}(4x) & \text{if } 0<x<0.125\\ 1 & \text{if } 0.125<x<0.875\\ w_{\mathrm{akaike}}\{4(x\text{-}0.750)\} & \text{if } 0.875<x<1\\ 0 & \text{else}\end{cases}, \tag{3}$$

where $w_{\mathrm{akaike}}(x)=0.625\text{-}0.5\cos\{2\pi x\}\text{-}0.125\cos\{4\pi x\}$ is the Akaike window. As a result, the diffraction pattern also decayed smoothly toward the outside without any

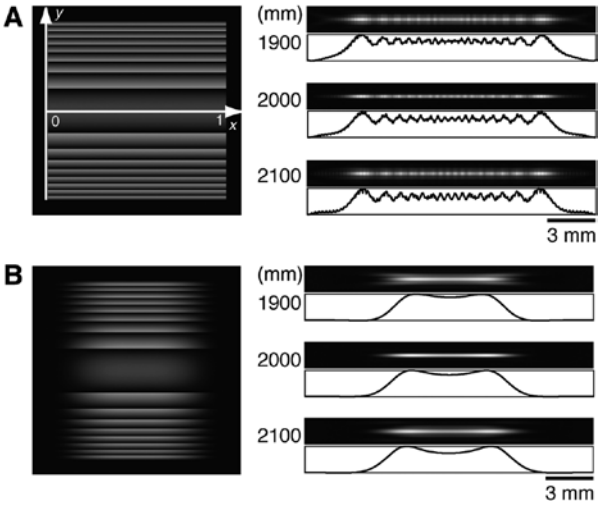

Figure 1: Phase distributions of holographic cylindrical lenses with (A) w_{rect} and (B) w_{mak} and their computational reconstructions at different distances from the SLM.

oscillations, as shown in Figure 1B. In a number of experimental trials undertaken to devise a better function, the window function w_{mak} produced a line-shaped beam that exhibited smooth changes.

2.2 Femtosecond laser processing system using line-shaped beams

Figure 2 shows the experimental setup. It was composed mainly of an amplified femtosecond laser system (Micra and Legend Elite, Coherent, Inc., Santa Clara, CA, USA), a liquid-crystal-on-silicon SLM (LCOS-SLM; X10468-02, Hamamatsu Photonics K.K., Hamamatsu, Shizuoka, Japan), laser processing optics, and a personal computer (PC; CPU, Intel Core i5 3.20 GHz, RAM, 2 GB). The femtosecond pulses with a center wavelength of λ_c=800 nm, a spectral width of 30 nm full width at half-maximum (FWHM), a pulse duration of 35 fs, a variable repetition frequency from 1 Hz to 1 kHz controlled by a Pockels cell in the laser

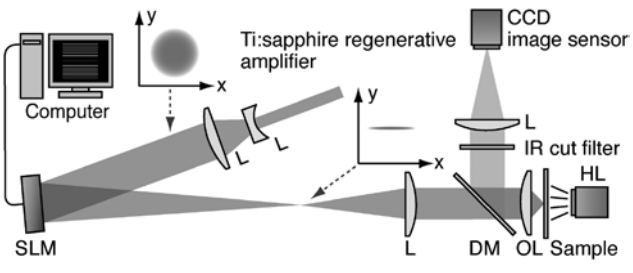

Figure 2: Femtosecond laser processing system using line-shaped beams.

system, and linear polarization were collimated, and the collimated beam illuminated the SLM. The beam was diffracted by a CGH, in this experiment a holographic cylindrical lens, displayed on the SLM and was transformed to a desired pattern (a line-shaped beam) at the desired plane. The line-shaped beam was imaged on the sample through reduction optics with a magnification M of 1.24×10^{-2} constructed from a 60× objective lens (OL) with an NA of 0.85 (focal length f=3.09 mm) and a lens (f=250 mm). The diameter of a beam incident on the pupil of an objective lens should be less than the pupil size because the diffraction on the edges of the objective lens appears in the hologram reconstruction. In our setup, the diameter of the incident beam was set to be less than the pupil size of the objective lens. The light-use efficiency was 25% at the focal plane of the cylindrical lens, 18% in front of the OL, and 8% behind the OL. The irradiation energy E was the total pulse energy of the diffracted beam at the sample plane, which was obtained as follows. First, the ratio between the energy split off by the DM and the energy at the sample plane was estimated. The total irradiation pulse energy was continuously monitored using a power meter, as the product of the energy split off by the DM and this ratio. To observe the laser processing of the sample, the sample was illuminated with a halogen lamp (HL), and a charge coupled device (CCD) image sensor captured images of the sample via a dichroic mirror (DM) and an infrared (IR) cut filter. The sample surface after laser processing was observed with a laser confocal microscope (OLS4000, Olympus Corporation, Tokyo, Japan) and a scanning electron microscope (SEM; FE-SEM S-4500, Hitachi, Ltd. Tokyo, Japan).

2.3 Laser peeling of ITO film

Figure 3 shows a wide laser peeling using a line-shaped beam generated by a holographic cylindrical lens. The sample was an indium tin oxide (ITO) film with a thickness of 10 nm coated on a glass substrate. Figure 3A shows an optical reconstruction of the holographic cylindrical lens with w_{mak} and its profile captured at the focal plane. The laser peeling shown in Figure 3B was performed with E=2.7 μJ, a pulse repetition frequency of 50 Hz, and a sample scanning speed of V_{scan}=2 μm/s. The threshold power for laser peeling of the ITO membrane, $E_{th}^{(ITO)}$, was 0.5 μJ, which was one sixth of the ablation threshold of the super white crown glass ($E_{th}^{(glass)}$=3.0 μJ). When E=1.4 μJ, at a scanning speed of V_{scan}=25 μm/s or higher (an irradiation interval of 500 nm), the ITO membrane was partially removed in the form of a periodical grating; that is, the peeling operation failed. When

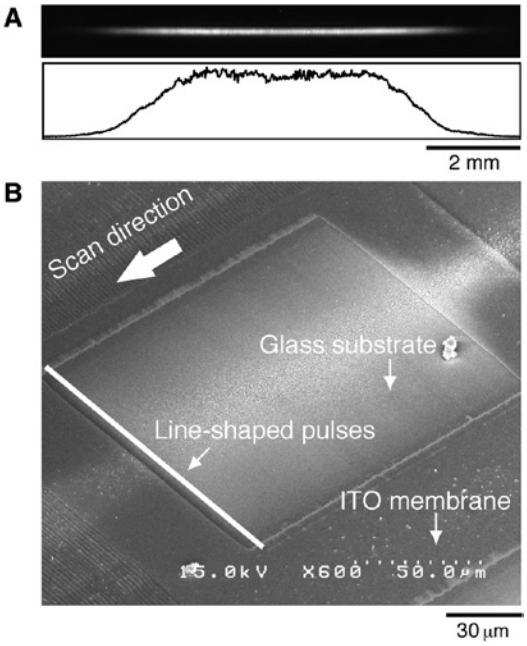

Figure 3: (A) Optical reconstruction of holographic cylindrical lens with w_{mak}. (B) Line-shaped laser peeling of ITO membrane on glass substrate.

E=2.7 μJ (10% smaller than the ablation threshold of the glass) at V_{scan}=25 μm/s, the ITO membrane was completely removed. When $E>E_{th}^{(glass)}$, the glass substrate was damaged, as expected. In summary, suitable conditions for laser peeling were an energy E slightly smaller than the ablation threshold of the substrate and an irradiation interval smaller than the width along the short axis (0.58 μm in this experiment).

Figure 4A and B depicts laser grooving on stainless steel, showing a confocal microscope image and the profile, respectively. The grooving was performed using a line-shaped beam with E=1.1 μJ and a pulse repetition frequency of 1 kHz, and V_{scan}=20 μm/s, generated by a holographic cylindrical lens with w_{mak}. In this case, linearly polarized light was used, and nanogratings with 500-nm spacing were observed, as shown in Figure 4C. When linearly polarized light with an azimuthal angle of 45° was used, we observed nanograting oriented in the perpendicular direction, as shown in Figure 4D. When circularly polarized light was used, no nanograting was formed, as shown in Figure 4E.

3 Large-scale holographic femtosecond laser processing using in-system CGH optimization

3.1 Principle of the in-system CGH optimization method

In order to perform large-scale holographic femtosecond laser processing with an enormous number of structures, optical reconstruction with uniform diffraction intensity from the CGH is essential. Therefore, the CGH should be sufficiently optimized. The optimal rotation angle (ORA) method [67] is an optimization algorithm designed to obtain the reconstruction of the CGH with uniform diffraction intensity. It is based on adding into the CGH an adequate phase variation obtained by an iterative optimization process. Although the ORA method allows us to design the high-quality CGH in the computer reconstruction, it is difficult to obtain the desired reconstruction in the real optical system due to the system's imperfections, including a characteristic of the SLM and an aberration of

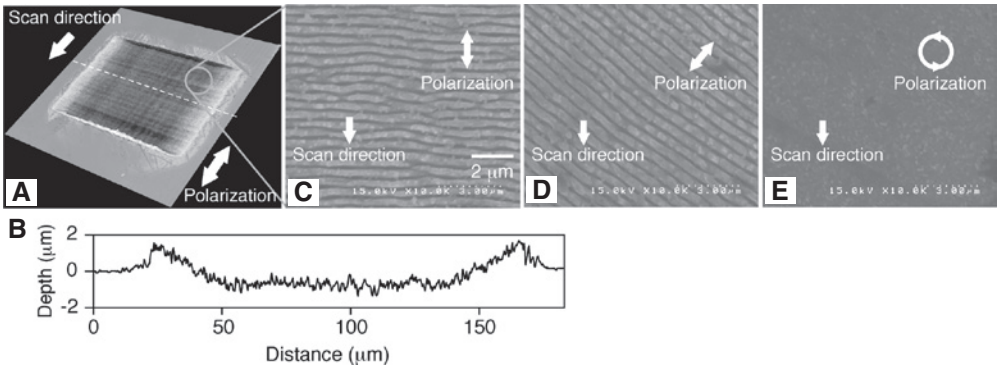

Figure 4: (A) Laser grooving of stainless steel with a line-shaped beam and (B) its depth profile. (C–E) SEM images of the structures processed with various polarizations.

the lenses. Therefore, the ORA method has been improved by taking into account an estimation of the optical reconstruction from the CGH [37], called an in-system optimization method. Accordingly, the improved ORA method has the capacity to eliminate the imperfections of the optical system.

In the *i*th iterative process, the relationship between an amplitude a_h and phase $\phi_h^{(i)}$ at a pixel *h* on the CGH plane, on the one hand, and a complex amplitude $U_r^{(i)}$ at a pixel *r* corresponding to the diffraction spot on the reconstruction plane, on the other hand, is described in the computer as follows:

$$U_r^{(i)} = \omega_r^{(i)} \sum_h u_{hr}^{(i)} = \omega_r^{(i)} \sum_h a_h \exp[i(\phi_{hr} + \phi_h^{(i)})], \tag{4}$$

where u_{hr} is the complex amplitude contributed from a pixel *h* on the CGH plane to a pixel *r* on the reconstruction plane, ϕ_{hr} is a phase contributed by the light propagation from a pixel *h* to a pixel *r*, and $\omega_r^{(i)}$ is a weight coefficient to control the diffraction light intensity at pixel *r*. In order to maximize the sum of the diffraction light intensity $\Sigma_r \left|U_r^{(i)}\right|^2$ at each pixel *r*, the phase variation $\Delta\phi_h^{(i)}$ added to $\phi_h^{(i)}$ at pixel *h* is calculated using following equations:

$$\begin{aligned} \Delta\phi_h^{(i)} &= \tan^{-1}(S_2 / S_1) \\ S_1 &= \sum_r \omega_r^{(i)} a_h \cos[\phi_r - (\phi_{hr} + \phi_h^{(i)})] \\ S_2 &= \sum_r \omega_r^{(i)} a_h \sin[\phi_r - (\phi_{hr} + \phi_h^{(i)})], \end{aligned} \tag{5}$$

where ϕ_r is the phase at pixel *r* on the reconstruction plane. The phase of CGH $\phi_h^{(i)}$ is updated by calculated $\Delta\phi_h^{(i)}$ as follows:

$$\phi_h^{(i+1)} = \phi_h^{(i)} + \Delta\phi_h^{(i)}. \tag{6}$$

Furthermore, in order to control the light intensity at pixel *r* on the reconstruction plane, $\omega_r^{(i)}$ is also updated based on an estimation of the optical reconstruction obtained in the actual setup using the following equation:

$$\omega_r^{(i+1)} = \omega_r^{(i)} \left(\frac{I_r^d}{I_r^{(i)}} \right)^{\alpha}, \tag{7}$$

where $I_r^{(i)} = \left|U_r^{(i)}\right|^2$ is the diffraction light intensity at pixel *r* in the optical reconstruction at the *i*th iterative process, I_r^d is the desired light intensity, and α is a constant. In the conventional ORA method, $I_r^{(i)}$ is typically the diffraction light intensity obtained in the computational reconstruction. The phase variation $\Delta\phi_h^{(i)}$ and the weight coefficient $\omega_r^{(i)}$ are continuously optimized by the above iterative process (Eqs. (5)–(7)) until $I_r^{(i)}$ is nearly equal to I_r^d. Consequently, the desired reconstruction is obtained in the optical setup.

3.2 Holographic femtosecond laser processing system using the in-system CGH optimization

Figure 5 shows the experimental setup. It was composed mainly of an amplified femtosecond laser system (Micra and Legend Elite, Coherent, Inc., Santa Clara, CA, USA), an LCOS-SLM (LCOS-SLM; X11840-02, Hamamatsu Photonics K.K., Hamamatsu, Shizuoka, Japan), laser processing optics, and a PC (CPU, Intel Core i5 3.20 GHz, RAM, 2 GB). The femtosecond pulse had a center wavelength of 800 nm, a spectral width of 8 nm FWHM, a pulse width of 110 fs, and a repetition frequency of 1 kHz. The pulse was irradiated onto a CGH displayed on the SLM through a reflection from a prism mirror (PM). The reconstructed spot array divided by a beam sampler (BS) was captured by a cooled CCD image sensor. The PC then evaluated the uniformity of the optical reconstruction from the captured image and recalculated the CGH using the ORA method with its evaluation. The optical reconstruction was sufficiently optimized until a uniform intensity in the array of spots was obtained, and it was directed to the laser processing optics, containing a 60× OL with NA=0.85. To observe the laser processing of the sample, the sample was illuminated with an HL, and a CCD image sensor captured images of the sample via a DM and an IR cut filter. The sample was super white crown glass (Schott B270). The irradiation pulse energy *E* represents the average energy of each spot on the sample plane and was obtained as follows. First, the ratio between the energy split off by the BS arranged in front of the SLM and the energy at the sample plane was estimated. The total irradiation pulse energy on the sample plane was continuously monitored using a power meter, as the product of the energy split off by the BS and this ratio. As a result, *E* is equal to the total irradiation energy divided by the number of diffraction spots. A pulse shot number was controlled by a mechanical shutter (SH). The sample surface after laser processing was observed with a transmitted optical microscope (BX-51, Olympus Corporation, Tokyo, Japan).

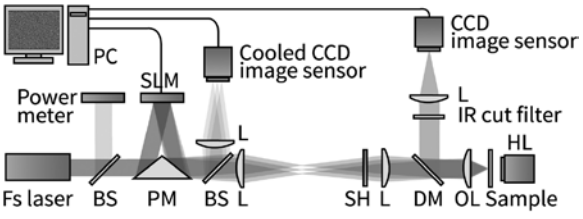

Figure 5: Holographic femtosecond laser processing system with the in-system CGH optimization.

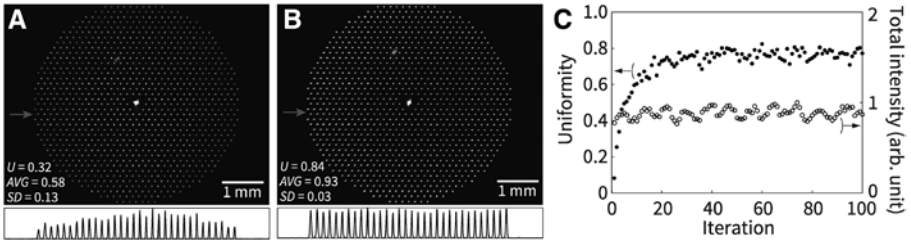

Figure 6: Optical reconstructions of the CGH obtained by (A) the conventional ORA method and (B) the in-system optimization method, respectively. (C) Change of the uniformity in the reconstruction of (B) vs. an iteration of the CGH optimization.

3.3 Large-scale holographic femtosecond laser processing

Figure 6A shows an optical reconstruction from the CGH optimized in the computer (the conventional ORA method) and its intensity profile on the line indicated by the gray arrow. The number of parallel beams was set to 1005. The central spot in the reconstruction represents the 0th order light. The uniformity U in the reconstruction was 0.32, where U was defined as the ratio of the maximum and minimum diffraction peak intensities in the reconstruction. The average (*AVG*) and the standard deviation (*SD*) of the peak intensity were 0.58 and 0.13, respectively. The quality of the reconstruction was rather insufficient. In particular, the intensity of the spots arranged on a high spatial frequency area (outside of the reconstruction) was obviously decreased by the spatial response characteristic of the SLM [35]. Figure 6B shows the optical reconstruction from the CGH obtained by the in-system optimization method (the improved ORA method mentioned above). U was 0.84. *AVG* and *SD* of the peak intensity were 0.93 and 0.03, respectively. Compared with the case of Figure 6A, the diffraction peak intensity arranged in the high frequency area was significantly enhanced. In Figure 6C, the filled circle shows the change of U in the reconstruction of Figure 6B vs. an iteration of the CGH optimization. The open circle shows the total intensity of the diffraction peaks in the CGH optimization. The total intensity was approximately maintained while improving the uniformity. The CGH optimization with 100 iterations required about 124 min in the case of a CGH with a pixel number of 800×600.

A reconstruction with an array of 1005 spots was applied to the laser processing of the glass surface. Figure 7A shows an optical microscope image of the structure processed by the optical reconstruction (Figure 6A) from the CGH obtained by the conventional ORA method. Figure 7B shows an optical microscope image of the structure processed by the optical reconstruction (Figure 6B) from the CGH obtained by the in-system optimization method. Each instance of processing was performed when E and the pulse shot number were set to 49 nJ and 5, respectively. The improvement of the quality of the fabricated structure was experimentally confirmed. Figure 7C shows the number of fabricated structures N_{struct} vs. E when the optical reconstructions corresponding to Figure 6A and B were used. In the case of the in-system CGH optimization method, N_{struct} changed more steeply with increasing E than it did in the case of the conventional ORA method. This is also evidence that the CGH reconstruction had high uniformity over a wide area because the slope depends on the spatial uniformity of the diffraction peak intensity,

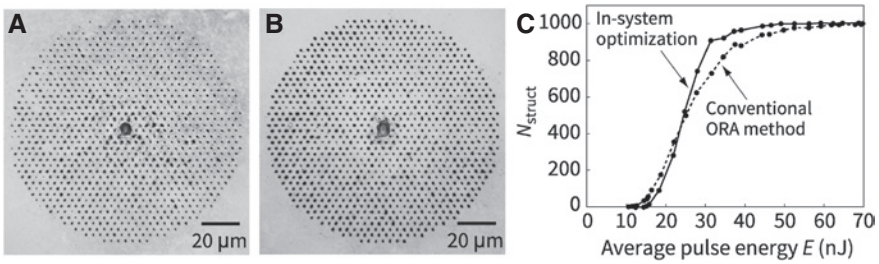

Figure 7: Optical microscope images of the processed structure with the CGH obtained by (A) the conventional ORA method and (B) the in-system optimization method, respectively. (C) Number of fabricated structures N_{struct} vs. the average pulse energy E when the CGHs were used.

in addition to the nonlinearity of laser processing. Furthermore, the E required to fabricate over 1000 pits was decreased from 70 to 49 nJ. This represents our first demonstration of large-scale holographic femtosecond laser processing using in-system CGH optimization.

4 Dynamic control of spatial wavelength dispersion in holographic femtosecond laser processing

4.1 Focal spot broadening due to wavelength dispersion of the CGH

Figure 8 schematically shows the optical system used for holographic femtosecond laser processing. A Fourier CGH displayed on an SLM, illuminated by a collimated femtosecond laser pulse with a center wavelength λ_c and spectral width $\Delta\lambda$, is imaged with magnification M (<1) at the pupil plane of an objective lens (OL) with a focal length f_{OL}, and the resulting diffraction pattern irradiates a sample placed at the Fourier plane of the imaged CGH. When the CGH has fringes with a spatial frequency ν, and the CGH is irradiated with a pulse of light with an incident angle of 0°, if $\nu\lambda_c$ is sufficiently smaller than 1, the diffraction position r is approximated as

$$r \approx f_{OL}\nu\lambda_c M. \tag{8}$$

Here, $M=f_2/f_1$, where f_1 and f_2 are the focal lengths of lenses 1 and 2, respectively. The maximum position, r_{max}, is determined by the maximum spatial frequency of the SLM, ν_{max}, and is given by $r_{max}=f_{OL}\nu_{max}\lambda_c M$. The focal spot broadening Δr is obtained from the derivative of Eq. (8):

$$\Delta r = f_{OL}\nu\Delta\lambda M. \tag{9}$$

From Eqs. (8) and (9), we obtain

$$\Delta r = \frac{\Delta\lambda}{\lambda_c} r. \tag{10}$$

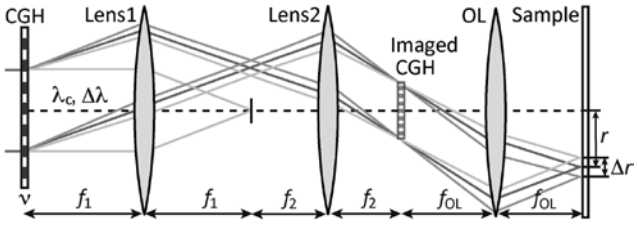

Figure 8: Schematic of focal spot broadening due to wavelength dispersion in holographic femtosecond laser processing.

This equation means that Δr depends on only r when a femtosecond laser pulse with given λ_c and $\Delta\lambda$ is supplied. The broadening Δr linearly increases with increasing r and $\Delta\lambda$. Consequently, Δr is independent of the optical setup parameters M and f_{OL} and of the spatial frequency ν of the CGH.

4.2 Principle of wavelength dispersion control using a pair of CGHs

Figure 9 shows an optical system designed to represent the principle of spatial wavelength dispersion control. In an ordinary system like that shown in Figure 8, when a collimated femtosecond laser pulse with a center wavelength λ_c, a spectral width $\Delta\lambda$, and an incident angle θ_{in} of 0° is irradiated onto a Fourier CGH with a center spatial frequency ν_{cgh}, the diffraction angle for λ_c is expressed as

$$\theta_c = \sin^{-1}(\nu_{cgh}\lambda_c) \tag{11}$$

in the case of paraxial analysis. Normally, the angular separation for $\Delta\lambda$ is equal to

$$\Delta\theta = \sin^{-1}(\nu_{cgh}\Delta\lambda), \tag{12}$$

which results in spatial broadening Δr of the focal spot at the diffraction position r on the focal plane, where r is defined as the horizontal distance from the 0th-order pulse. To compensate for Δr due to wavelength dispersion, a spectrally dispersed femtosecond pulse with a different incidence angle θ_{in} for each λ is irradiated onto the CGH, as shown in Figure 9. The incidence angle for each λ is expressed using the grating equation

$$\theta_{in}(\lambda) = \sin^{-1}[\nu_{grat}(\lambda-\lambda_c)] + \sin^{-1}(\nu_{grat}\lambda_c). \tag{13}$$

This dispersed femtosecond pulse with incidence angle θ_{in} is generated by a grating with spatial frequency ν_{grat} arranged in a *2f-2f* setup. Owing to the dispersed pulse irradiation, the angular separation of the diffraction pulse

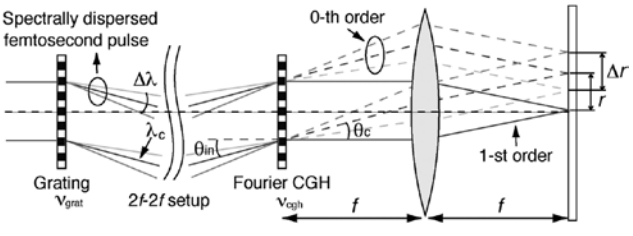

Figure 9: Schematic of wavelength dispersion control using a pair of CGHs. The solid and broken lines represent the 1st- and 0th-order pulses, respectively, diffracted by the CGH.

is compensated for and is effectively given away to the 0th-order pulse. When ν_{grat} and ν_{cgh} are changed simultaneously and dynamically, the focusing position of the 0th-order pulse is also changed. The dynamical change of the 0th pulse is very effective in cases where it is difficult to completely eliminate undesired processing by the 0th-order pulse.

4.3 Holographic femtosecond laser processing system with wavelength dispersion control

Figure 10 shows the experimental setup. It was composed mainly of an amplified femtosecond laser system (Micra and Legend Elite, Coherent, Inc., Santa Clara, CA, USA), LCOS-SLMs (LCOS-SLM; X10468-02, Hamamatsu Photonics K.K., Hamamatsu, Shizuoka, Japan), laser processing optics, and a PC. The femtosecond pulses from the laser system had a center wavelength λ_c of 800 nm, a spectral width $\Delta\lambda$ of 30 nm FWHM, and a repetition frequency of 1 kHz. The pulse width was 50 fs at the sample plane. To compensate for the angular separation of the diffraction pulse, the pulse was first irradiated onto the SLM1 displaying the CGH1 designed to generate a spectrally dispersed pulse. To reconstruct the parallel beams, the pulse was irradiated onto the SLM2 displaying the CGH2 designed to diffract the incoming pulse. The reconstructed spot array was directed to the laser processing optics, composed of an OL (NA=0.45). To observe the processing results, the sample was illuminated from behind with an HL, and a CCD image sensor captured images of the sample via a DM and an IR cut filter. The sample was a piece of fused silica. The irradiation energy E was the average energy of each diffraction pulse at the sample plane. The sample surface after laser processing was observed with a transmitted optical microscope (BX-51, Olympus Corporation, Tokyo, Japan).

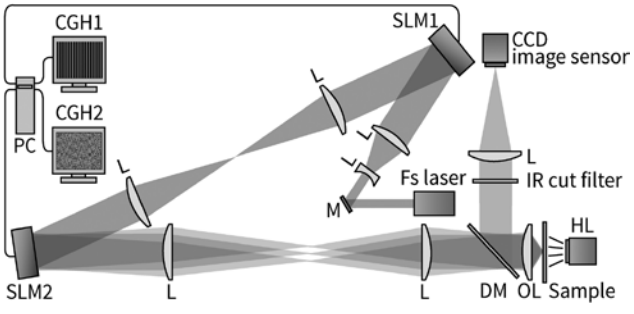

Figure 10: Holographic femtosecond laser processing system with wavelength dispersion control.

4.4 Holographic femtosecond laser processing with dynamic control of wavelength dispersion

Holographic femtosecond laser processing was demonstrated on fused silica using the reconstructed spot arrays both without and with dynamic control of spatial wavelength dispersion. Figure 11 shows the transmission optical microscope images of the fabricated structure. The structure was composed of dot structures of 8151 points. Processing was performed by switching the CGHs displayed on the SLM2 without mechanical scanning. Each CGH reconstructed 30 parallel pulses and simultaneously fabricated 30 dots with single-shot irradiation. The pulse repetition rate was set to 10 Hz. The processing time for each demonstration was about 27 s. Figure 11A is an image of the structure fabricated with a single SLM2 displaying the CGHs, which reconstructed the parallel pulses arranged around the 0th-order pulse. In the image, the square indicates the position of the 0th-order pulse irradiation, that is, an optical axis. E was 1.14 μJ. Unnecessary processing given by the 0th-order pulse appears at the center of the structure.

To separate the processing by the 0th-order pulse from the structure, the CGHs, which reconstructed the parallel pulses arranged separately from the 0th-order pulse, were used. The CGHs were designed by superposing a grating with a spatial frequency ν of 9.8 lp/mm and an orientation of 90° on the original CGHs shown in Figure 11A. Figure 11B is an image of the structure fabricated with a single SLM2 displaying the CGHs. In the image, the inserted square area represents the position of the 0th-order pulse irradiation, that is, an optical axis. Although processing by the 0th-order pulse was separated from the structure, the spatial resolution of the structure was significantly decreased due to the influence of spatial wavelength dispersion on the reconstruction. In addition, the E required to fabricate the structure was 2.15 μJ and 1.9 times larger than the result of Figure 11A.

To control spatial wavelength dispersion and avoid the processing by the 0th-order pulse, two SLMs were used. The SLM2 displayed the CGHs designed by superposing gratings with ν of 9.8 lp/mm and an orientation of 80°–100° on the original CGHs shown in Figure 11A. The SLM1 was used to control dispersion and displayed the gratings with the same ν and the opposite orientation for the gratings superposed on the CGHs displayed on the SLM2. The orientation of the superposed grating determined the position relationship between the 0th-order and 1st-order pulse. Therefore, the grating with a variety of the orientation enabled us to arbitrarily

Figure 11: Transmission optical microscope images of the fabricated structure. The structure fabricated with (A) a single SLM2 displaying the CGHs, which reconstructed the parallel pulses arranged around the 0th-order pulse, (B) a single SLM2 displaying the CGHs, which reconstructed the parallel pulses arranged separately from the 0th-order pulse, and (C) a pair of SLMs. Inserted square and rectangle areas represent the position of the 0th-order pulse irradiation.

change the position of the 0th-order pulse. Figure 11C is an image of the structure fabricated with a pair of SLMs. In the image, the inserted rectangle area represents the position of the 0th-order pulse irradiation. An optical axis was the center of structure. E was 1.40 μJ. By the dynamic control of spatial wavelength dispersion, the dispersion was effectively given away to the 0th order. Furthermore, the position of the 0th-order pulse irradiation was moved slightly at the bottom to upper inside the rectangle area in each pulse shot. Therefore, the unnecessary processing given by the 0th-order pulse was perfectly restrained.

5 Holographic vector-wave femtosecond laser processing

5.1 Principle of vector-wave control using the CGH

Conventional holographic femtosecond laser processing employs the basic principle of wavefront modulation using a CGH. However, full control of degrees of freedom in the light, including amplitude, phase, and polarization, is important for opening up a wide variety of new applications of femtosecond laser processing. Such control entails exploiting the nature of light as a vector wave and is known as vector-wave control.

The optical setup for vector-wave control consists mainly of a half-wave plate (HWP), a quarter-wave plate (QWP), and a pair of SLMs. When the Jones matrixes of these optical elements are defined as H, Q, and S, respectively, the Jones vector of the output beam from the setup, $\mathbf{E}_{\text{out}}$, is expressed as

$$\begin{aligned}\mathbf{E}_{\text{out}} &= Q_{\frac{\pi}{4}} S_{\beta} H_{\frac{\pi}{8}} S_{\alpha} \mathbf{E}_{\text{in}} \\ &= \frac{1}{2}\begin{bmatrix} -i\exp[i(\alpha+\beta)]+\exp(i\alpha) & i\exp(i\beta)+1 \\ -\exp[i(\alpha+\beta)]+i\exp(i\alpha) & \exp(i\beta)+i \end{bmatrix}\mathbf{E}_{\text{in}} \\ &= \frac{\exp(i\alpha)}{2}\begin{bmatrix} -i\cos\beta+\sin\beta+1 \\ -\cos\beta-i\sin\beta+i \end{bmatrix}, \end{aligned} \tag{14}$$

where $\mathbf{E}_{\text{in}}=(1,0)^{\text{T}}$ is the Jones vector of an input beam with linear polarization, the subscripts on H and Q are the azimuthal angles at the respective wave plates, and the subscripts α and β are the phases applied to the pair of SLMs, respectively. As shown in Eq. (14), wavefront modulation and polarization modulation of the output beam are independently controlled by phases α and β, respectively. These controls correspond to the array arrangement of the spots and its polarization, respectively. Figure 12 shows the polarization direction of the output beam vs. phase β from Eq. (14). In the figure, the slope and y-intercept are set to 1/2 and $-\pi/4$ in our setup, respectively.

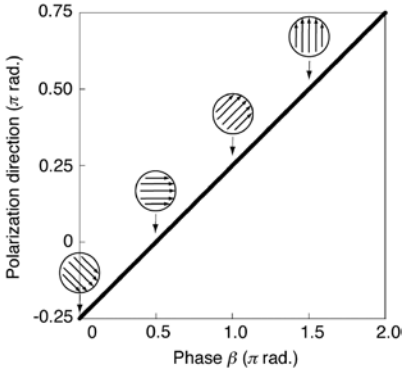

Figure 12: Polarization direction of output beam vs. phase β applied to the SLM.

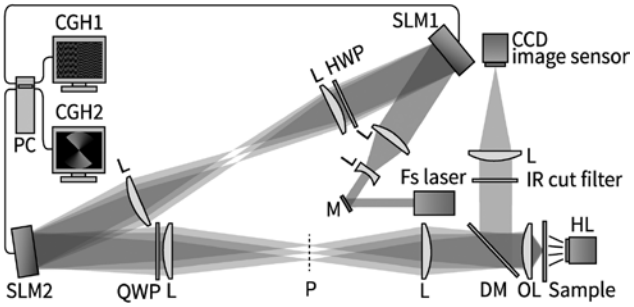

Figure 13: Holographic vector-wave femtosecond laser processing system.

5.2 Holographic vector-wave femtosecond laser processing system

Figure 13 shows the experimental setup. It was composed mainly of an amplified femtosecond laser system (Micra and Legend Elite, Coherent, Inc., Santa Clara, CA, USA), LCOS SLMs (LCOS-SLM; X10468-02, Hamamatsu Photonics K.K., Hamamatsu, Shizuoka, Japan), laser processing optics, and a PC. The incident femtosecond pulse had a center wavelength of 800 nm, a spectral width of 25 nm FWHM, a pulse width of 40 fs, a repetition frequency of 1 kHz, and a linear polarization with a p-component. The pulse was irradiated onto the first SLM (SLM1), which displayed the CGH1 designed to apply a pure phase delay to the p-component, that is, wavefront modulation. The HWP was arranged with an azimuthal angle of $\pi/8$ to rotate the linear polarization by $\pi/4$. The pulse was also irradiated onto the second SLM (SLM2), which displayed the CGH2 designed to apply a phase delay between the p- and s-components, that is, polarization modulation. The SLM2 was located at the image plane of the SLM1. The circular or elliptical polarization reflected from the SLM2 was converted to linear polarization using a QWP set to an azimuthal angle of $\pi/4$. Consequently, the reconstructed spot array with the desired polarization distribution was obtained at plane P and was directed to the laser processing optics, containing a 40× OL with NA=0.60. To observe the laser processing of the sample, the sample was illuminated with HL, and a CCD image sensor captured images of the sample via a DM and an IR cut filter. The sample was super white crown glass (Schott, B270). The structure fabricated by the laser irradiation was observed using a transmitted optical microscope (BX-51, Olympus Corporation, Tokyo, Japan) and an SEM (SEM; FE-SEM S-4500, Hitachi, Ltd. Tokyo, Japan).

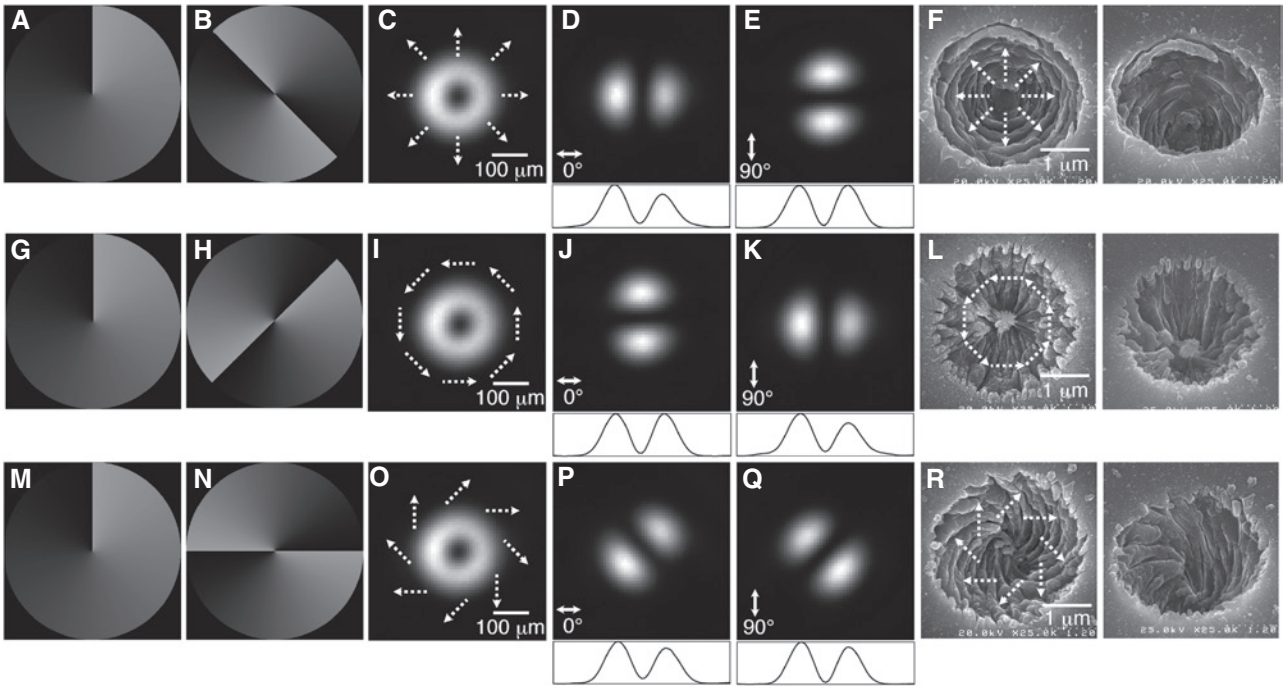

Figure 14: Typical cases of a cylindrical vector beam. (A–F) The case of a radial polarization beam. The CGHs for (A) wavefront modulation, (B) polarization modulation, and (C) their respective optical reconstructions. Reconstructions through a polarizer with an azimuthal angle of (D) 0° and (E) 90°, respectively. (F) SEM images from a top and bird's eye view of the fabricated structure. (G–L) The case of an azimuth polarization beam. (M–R) The case of a windmill polarization beam.

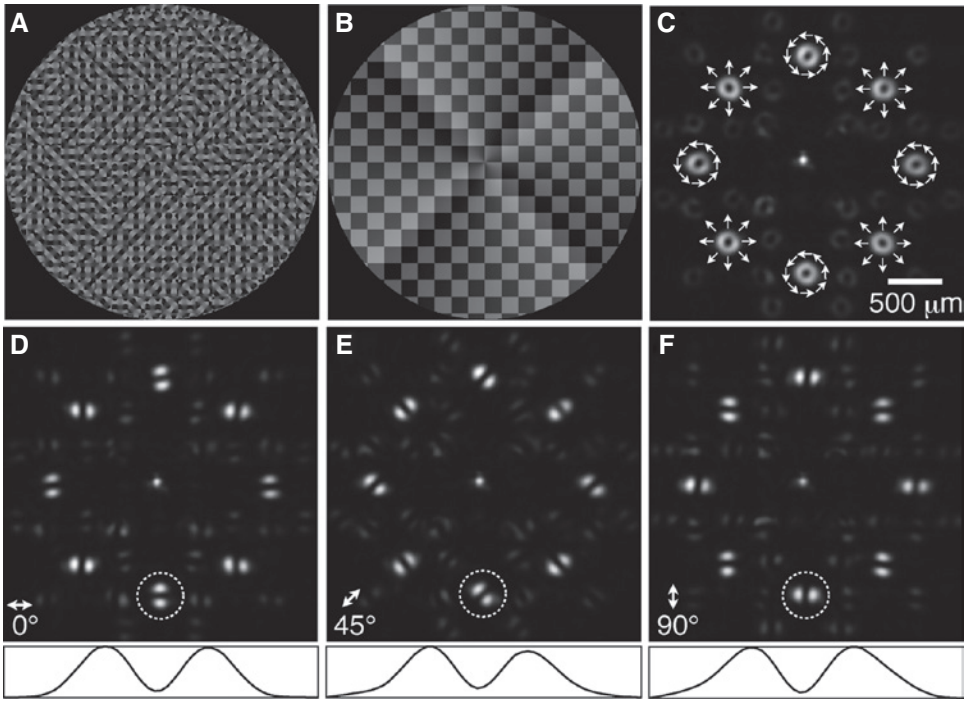

Figure 15: CGHs for modulating (A) wavefront and (B) polarization state, respectively. (C) Optical reconstruction of multifocal radial and azimuth beams. The reconstructions were captured through a linear polarizer with azimuthal angles of (D) 0°, (E) 45°, and (F) 90°, respectively.

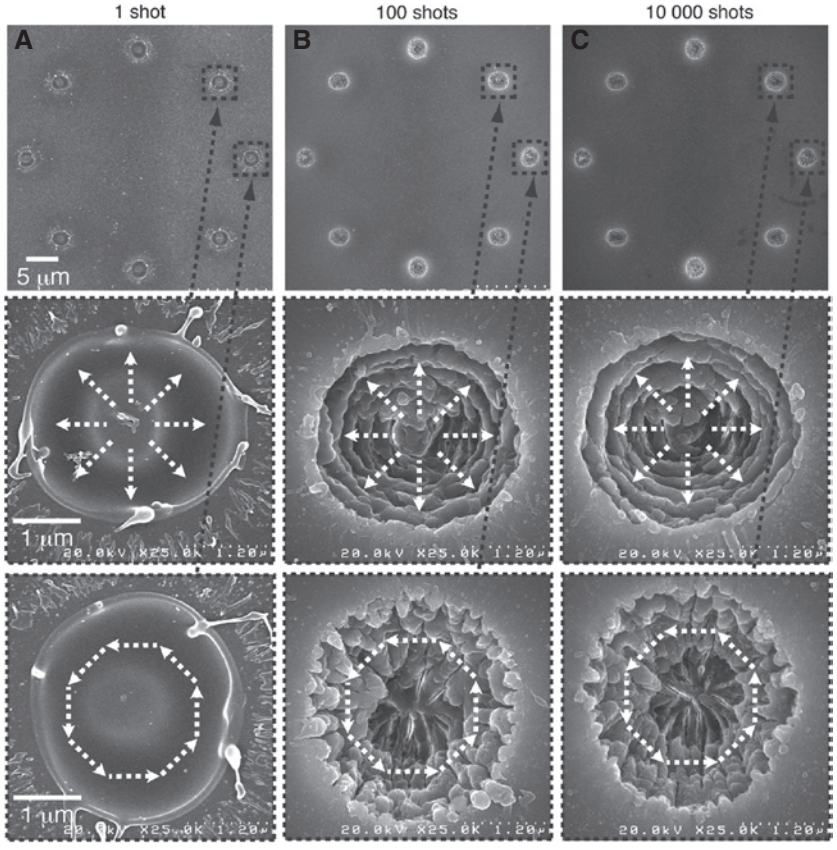

Figure 16: SEM images of the structure fabricated using multifocal radial and azimuth beams with a pulse shot number of (A) 1, (B) 100, and (C) 10,000, respectively.

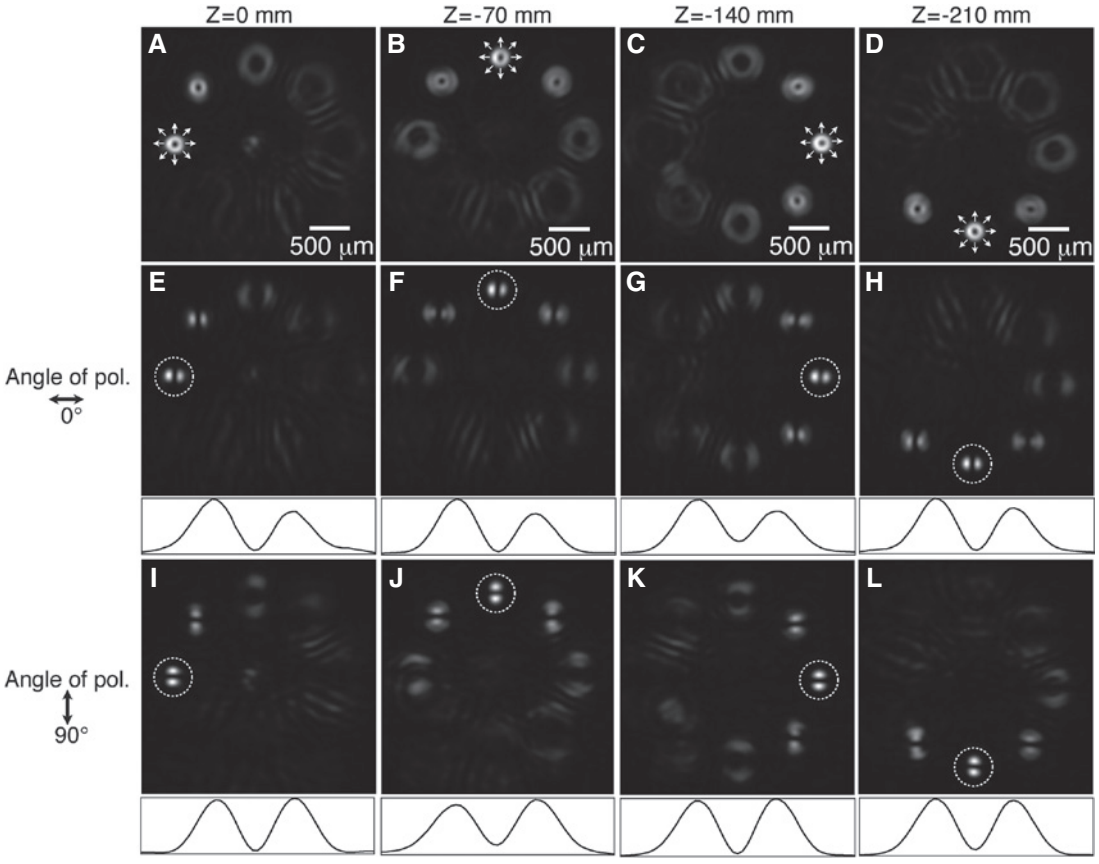

Figure 17: A 3D optical reconstruction of multifocal radial beams captured at (A) z=0, (B) -70, (C) -140, and (D) -210 mm, respectively. The reconstructions were captured through a linear polarizer with an azimuthal angle of (E–H) 0 and (I–L) 90° at z=0, -70, -140, and -210 mm, respectively.

5.3 Fabrication of orientation-controlled nanostructures using holographic vector-wave femtosecond laser processing

Figure 14 shows typical cases of a single cylindrical vector beam. Figure 14A–F shows the case of a radial polarization beam. Figure 14A and B shows CGHs for wavefront and polarization modulation, respectively. The gray scale corresponds to the phase from 0 to 2π. Figure 14C–E depicts the optical reconstruction captured at plane P in Figure 13 through a polarizer with the azimuthal angles of 0° and 90° and its intensity profiles, respectively. In the figure, white arrows represent the polarization direction. The reconstruction had a doughnut-shaped intensity at focus because each focal spot had a phase and polarization singularity at the beam center. Figure 14F shows SEM images from a top and bird's eye view of the structure fabricated by the vector beam. Processing was performed with a pulse energy of 270 nJ and a pulse shot number of 10,000. The pitch of the fabricated nanostructure was approximately 180 nm. The orientation of the nanostructure was coincident with the polarization state of the vector beam. Figure 14G–L shows the case of an azimuth polarization beam. Figure 14M–R shows the case of a windmill polarization beam. Interestingly, a vortical nanostructure was successfully fabricated. From each SEM image with a bird's eye view, three different types of spatially complex nanostructures were fabricated on the sidewall of the hole by controlling the polarization state of the beam using the CGH.

Figure 15A and B shows CGHs designed to modulate the wavefront and the polarization state of the light in order to reconstruct the multifocal radial and azimuth beams, respectively. These CGHs were organized such that small square CGHs, which reconstructed the multifocal radial and azimuth beams, were alternately arranged [60]. Figure 15C shows the optical reconstruction. Figure 15D–F shows the reconstructions captured through a linear polarizer with azimuthal angles of 0°, 45°, and 90°, respectively. The profiles represent the intensity distribution corresponding to the focal spot inside the dashed circle. The results demonstrate that the simultaneous reconstruction of two different types of multifocal vector beams was successfully performed.

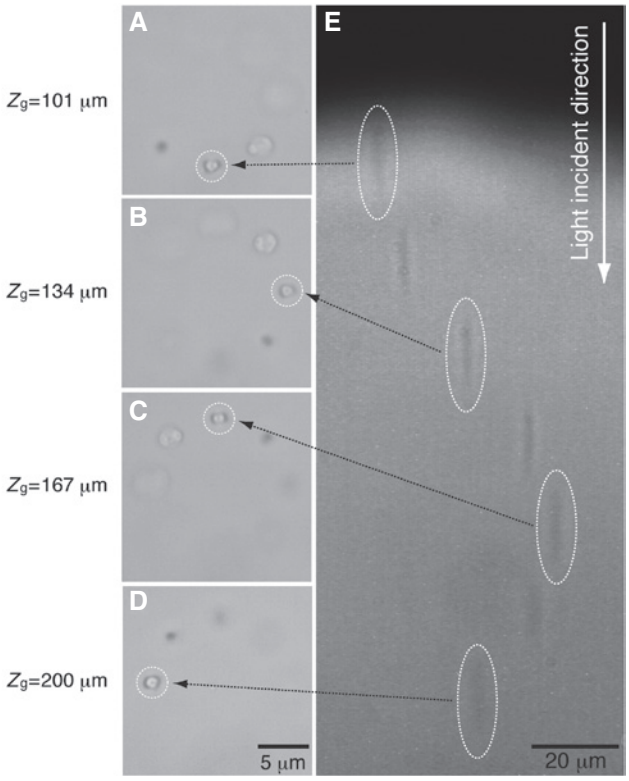

Figure 18: Transmitted optical microscope images of the helical structure at a depth of (A) 101, (B) 134, (C) 167, and (D) 200 μm fabricated inside a piece of glass by 3D multifocal radial beams, respectively. z_g is the depth from the glass surface. (E) Side view image of the fabricated structure.

In order to confirm the polarization states of the spot at the sample plane (the focal plane of the objective lens), laser processing was performed, and the polarization state was analyzed from the orientations of the fabricated nanostructures. Figure 16A–C shows SEM images of the structure fabricated using the reconstruction depicted in Figure 15C and its magnified images at each location when the pulse energy E was set to 0.88, 0.59, and 0.59 μJ, respectively, and the pulse shot number was set to 1100, and 10,000, respectively. The results demonstrate that the orientation of the fabricated nanostructures agreed well with the polarization state of each beam. Furthermore, two different types of spatially complex nanostructures with a pitch of 150 nm were simultaneously fabricated.

A 3D reconstruction of multifocal radial beams was also demonstrated. Figure 17A–D shows the optical reconstructions captured at z=0, -70, -140, and -210 mm, respectively, where z is the distance from the Fourier plane of the CGH (plane P in Figure 13). Figure 17E–H and I–L shows the reconstructions captured through a linear polarizer with an azimuthal angle of 0° and 90° at z=0, -70, -140, and -210 mm, respectively. The profiles represent the intensity distribution corresponding to the focal spot inside the dashed circle. In each captured plane, one beam was successfully focused while maintaining radial polarization.

The 3D optical reconstruction of multifocal radial beams was applied to laser processing inside a piece of glass. Figure 18A and D shows transmitted optical microscope images of the fabricated structure focused on inside a piece of glass at a depth z_g of 101, 134, 167, and 200 μm, respectively, where z_g=0 represents the glass surface. The pulse energy E and the pulse shot number were set to 0.63 μJ and 10,000, respectively, during processing. Figure 18E is a transmitted optical microscope image of a side view of the fabricated structure. The results demonstrate that the 3D helical structure was successfully fabricated with multifocal radial beams.

6 Conclusion

We summarized some of our experimental results from the past few years regarding holographic femtosecond laser manipulation for advanced material processing. In particular, line-shaped and vector-wave femtosecond laser processing based on holographic manipulation of the wavefront and polarization of the light were demonstrated. These beam-shaping techniques are useful for performing large-area machining and high-speed fabrication of the complex nanostructures applied to material-surface texturing. In addition, issues related to the nonuniformity of diffraction light intensity in optical reconstruction and wavelength dispersion from the CGH were addressed. Consequently, large-scale holographic femtosecond laser processing over 1000 diffraction spots was successfully demonstrated.

Acknowledgments: This study was supported by a Grant-in-Aid for Scientific Research (B), by a Grant-in-Aid for Challenging Exploratory Research from the Ministry of Education, Culture, Sports, Science, and Technology of Japan, and by Nippon Sheet Glass Foundation for Materials Science and Engineering.

References

[1] D. Du, X. Liu, G. Korn and G. Mourou, Appl. Phys. Lett. 64, 3071–3073 (1994).
[2] H. Kumagai, K. Midorikawa, K. Toyoda, S. Nakamura, T. Okamoto, et al., Appl. Phys. Lett. 65, 1850–1852 (1994).
[3] K. Kawamura, T. Ogawa, N. Sarukura, M. Hirano and H. Hosono, Appl. Phys. B. 71, 119–121 (2000).

[4] T. Kondo, S. Matsuo, S. Juodkazis and H. Misawa, Appl. Phys. Lett. 79, 725–727 (2001).
[5] Y. Li, W. Watanabe, K. Yamada, T. Shinagawa, K. Itoh, et al., Appl. Phys. Lett. 80, 1508–1510 (2002).
[6] S. Matsuo, S. Juodkazis and H. Misawa, Appl. Phys. A 80, 683–685 (2005).
[7] J. Kato, N. Takeyasu, Y. Adachi, H.-B. Sun and S. Kawata, Appl. Phys. Lett. 86, 044102 (2005).
[8] J. Amako, K. Nagasaka and N. Kazuhiro, Opt. Lett. 27, 969–971 (2002).
[9] Y. Kuroiwa, N. Takeshima, Y. Narita, S. Tanaka and K. Hirao, Opt. Express 12, 1908–1915 (2004).
[10] Y. Hayasaki, T. Sugimoto, A. Takita and N. Nishida, Appl. Phys. Lett. 87, 031101 (2005).
[11] N. Sanner, N. Huot, E. Audouard, C. Larat, J. P. Huignard, et al., Opt. Lett. 30, 1479–1481 (2005).
[12] S. Hasegawa, Y. Hayasaki and N. Nishida, Opt. Lett. 31, 1705–1707 (2006).
[13] L. Kelemen, S. Valkai and P. Ormos, Opt. Express 15, 14488–14497 (2007).
[14] H. Takahashi, S. Hasegawa, A. Takita and Y. Hayasaki, Opt. Express 16, 16592–16599 (2008).
[15] K. Obata, J. Koch, U. Hinze and B. N. Chichkov, Opt. Express 18, 17193–17200 (2010).
[16] S. D. Gittard, A. Nguyen, K. Obata, A. Koroleva, R. J. Narayan, et al., Biomed. Opt. Express 2, 3167–3178 (2011).
[17] Y. C. Li, L. C. Cheng, C. Y. Chang, C. H. Lien, P. J. Campagnola, et al., Opt. Express 20, 19030–19038 (2012).
[18] C. Mauclair, G. Cheng, N. Huot, E. Audouard, A. Rosenfeld, et al., Opt. Express 17, 3531–3542 (2009).
[19] M. Sakakura, T. Sawano, Y. Shimotsuma, K. Miura and K. Hirao, Jpn J. Appl. Phys. 48, 126507–126511 (2009).
[20] M. Sakakura, T. Sawano, Y. Shimotsuma, K. Miura and K. Hirao, Opt. Express 18, 12136–12143 (2010).
[21] M. Sakakura, T. Sawano, Y. Shimotsuma, K. Miura and K. Hirao, Opt. Lett. 36, 1065–1067 (2011).
[22] D. Liu, Z. Kuang, W. Perrie, P. J. Scully, A. Baum, et al., Appl. Phys. B 101, 817–823 (2010).
[23] H. Imamoto, S. Kanehira, X. Wang, K. Kametani, M. Sakakura, et al., Opt. Lett. 36, 1176–1178 (2011).
[24] M. Antkowiak, M. L. Torres-Mapa, F. Gunn-Moore and K. Dholakia, J. Biophotonics 3, 696–705 (2010).
[25] M. Yamaji, H. Kawashima, J. Suzuki and S. Tanaka, Appl. Phys. Lett. 93, 041116 (2008).
[26] M. Yamaji, H. Kawashima, J. Suzuki, S. Tanaka, M. Shimizu, et al., J. Appl. Phys. 111, 083107 (2012).
[27] M. K. Bhuyan, F. Courvoisier, P. A. Lacourt, M. Jacquot, R. Salut, et al., Appl. Phys. Lett. 97, 081102 (2010).
[28] A. Jesacher and M. J. Booth, Opt. Express 18, 21090–21099 (2010).
[29] B. P. Cumming, A. Jesacher, M. J. Booth, T. Wilson and M. Gu, Opt. Express 19, 9419–9425 (2011).
[30] S. Hasegawa and Y. Hayasaki, Opt. Express 23, 23185–23194 (2015).
[31] Z. Kuang, W. Perrie, J. Leach, M. Sharp, S. Edwardson, et al., Appl. Surf. Sci. 255, 2284–2289 (2008).
[32] Z. Kuang, D. Liu, W. Perrie, S. Edwardson, M. Sharp, et al., Appl. Surf. Sci. 255, 6582–6588 (2009).
[33] P. S. Salter and M. J. Booth, Opt. Lett. 36, 2302–2304 (2011).
[34] H. Takahashi, S. Hasegawa and Y. Hayasaki, Appl. Opt. 46, 5917–5923 (2007).
[35] K. Chaen, H. Takahashi, S. Hasegawa and Y. Hayasaki, Opt. Commun. 280, 165–172 (2007).
[36] S. Hasegawa and Y. Hayasaki, Opt. Rev. 14, 208–213 (2007).
[37] S. Hasegawa and Y. Hayasaki, Opt. Lett. 34, 22–24 (2009).
[38] S. Hasegawa and Y. Hayasaki, Jpn. J. Appl. Phys. 48, 09LE03 (2009).
[39] S. Hasegawa and Y. Hayasaki, Opt. Lett. 36, 2943–2945 (2011).
[40] Y. Hayasaki, M. Nishitani, H. Takahashi, H. Yamamoto, A. Takita, et al., Appl. Phys. A 107, 357–362 (2012).
[41] S. Hasegawa and Y. Hayasaki, Appl. Phys., A Mater. Sci. Process. 111, 929–934 (2013).
[42] I. G. Mariyenko, J. Strohaber and C. J. G. J. Uitenvaal, Opt. Express 13, 7599–7608 (2005).
[43] G. Mínguez-Vega, J. Lancis, J. Caraquitena, V. Torres-Company and P. Andrés, Opt. Lett. 31, 2631–2633 (2006).
[44] G. Mínguez-Vega, E. Tajahuerce, M. Fernández-Alonso, V. Climent, J. Lancis, et al., Opt. Express 15, 278–288 (2007).
[45] L. Martínez-León, P. Clemente, E. Tajahuerce, G. Mínguez-Vega, O. Mendoza-Yero, et al., Appl. Phys. Lett. 94, 011104 (2009).
[46] R. Martínez-Cuenca, O. Mendoza-Yero, B. Alonso, I. J. Sola, G. Mínguez-Vega, et al., Opt. Lett. 37, 957–959 (2012).
[47] S. Hasegawa and Y. Hayasaki, Opt. Lett. 39, 478–481 (2014).
[48] L. Novotny, M. R. Beversluis, K. S. Youngworth and T. G. Brown, Phys. Rev. Lett. 86, 5251–5254 (2001).
[49] K. Yoshiki, M. Hashimoto and T. Araki, Jpn. J. Appl. Phys. 44, L1066–L1068 (2005).
[50] B. Jia, H. Kang, J. Li and M. Gu, Opt. Lett. 34, 1918–1920 (2009).
[51] Y. Shimotsuma, P. G. Kazansky, J. Qiu and K. Hirao, Phys. Rev. Lett. 91, 247405 (2003).
[52] V. G. Niziev and A. V. Nesterov, J. Phys. D 32, 1455–1461 (1999).
[53] M. Meier, V. Romano and T. Feurer, Appl. Phys., A Mater. Sci. Process. 86, 329–334 (2007).
[54] O. J. Allegre, W. Perrie, S. P. Edwardson, G. Dearden and K. G. Watkins, J. Opt. 14, 085601 (2012).
[55] Y. Kozawa and S. Sato, Opt. Express 18, 10828–10833 (2010).
[56] S. Hasegawa and Y. Hayasaki, Opt. Express 21, 12987–12995 (2013).
[57] K. Lou, S. X. Qian, X. L. Wang, Y. Li, B. Gu, et al., Opt. Express 20, 120–127 (2012).
[58] Y. Jin, O. J. Allegre, W. Perrie, K. Abrams, J. Ouyang, et al., Opt. Express 21, 25333–25343 (2013).
[59] K. Lou, S. X. Qian, Z. C. Ren, C. H. Tu, Y. N. Li, et al., Sci. Rep. 3, 2281 (2013).
[60] O. J. Allegre, Y. Jin, W. Perrie, J. Ouyang, E. Fearon, et al., Opt. Express 21, 21198–21207 (2013).
[61] S. Hasegawa and Y. Hayasaki, Int. J. Optomechatronics, 8, 73–88 (2014).
[62] J. Bonse, R. Koter, M. Hartelt, D. Spaltmann, S. Pentzien, et al., Appl. Phys. A 117, 103–110 (2014).
[63] A. Y. Vorobyev and C. Guo, Opt. Express 18, 6455–6460 (2010).
[64] A. Y. Vorobyev and C. Guo, Opt. Express 19, A1031–A1036 (2011).
[65] M. Gecevičius, M. Beresna and P. G. Kazansky, Opt. Lett. 38, 4096–4099 (2013).
[66] K. Sakuma, S. Hasegawa, H. Takahashi, M. Ota and Y. Hayasaki, Appl. Phys. B, 119, 533–538 (2015).
[67] J. Bengtsson, Appl. Opt. 33, 6879–6884 (1994).

Satoshi Hasegawa
Center for Optical Research and Education (CORE), Utsunomiya University
7-1-2 Yoto, Utsunomiya 321-8585, Japan
hasegawa_s@opt.utsunomiya-u.ac.jp

Satoshi Hasegawa is an Assistant Professor at Department of Optical Engineering, Utsunomiya University, Japan. He received his master's degree from The University of Tokushima in 2007 and his doctorate degree from Utsunomiya University in 2010. He was a postdoctoral fellow at Center for Optical Research and Education (CORE), Utsunomiya University, until 2014. His current interests include femtosecond laser material processing with holographic manipulation and computer-generated holography.

Yoshio Hayasaki
Center for Optical Research and Education (CORE), Utsunomiya University, 7-1-2 Yoto
Utsunomiya 321-8585, Japan

Yoshio Hayasaki received his PhD (Applied Physics) from University of Tsukuba, Japan, in 1993. He was a researcher in RIKEN from April 1993 to March 1995. He was an Associate Professor in The University of Tokushima from April 1995 to March 2008. At present, he is a professor in Utsunomiya University, Center for Optical Research and Education (CORE). The main research fields are information photonics, optical metrology, and laser material processing. Recently, he is focusing on a holographic femtosecond laser processing, digital super-resolution microscopy, and optical frequency comb imaging.